Development of thin deformable X-ray mirrors for synchrotron applications

Xiaoya Chong¹, Kenneth M. Buffo², Philip Griffin², Pannawit Tipsawat³, Casey DeRoo², Susan Trolier-McKinstry³, Bryan Ochoa¹, Diane Bryant¹, Morgan Ericksen¹, Ali Sabbah¹, Nicolás Smith¹, Ian Lacey¹, Valeriy Yashchuk¹, Kenneth A. Goldberg¹, and Antoine Islegen-Wojdyla^{1,*}

¹Advanced Light Source, Lawrence Berkeley National Laboratory, Berkeley, California (USA)

²Department of Physics and Astronomy, University of Iowa, Iowa City, Iowa (USA)

³Department of Materials Science and Engineering, Pennsylvania State University, University

Park, Pennsylvania (USA)

ABSTRACT

The future of synchrotron light sources will bring diffraction-limited X-ray beams, providing high brightness and coherent wavefronts to an increasing number of beamline endstations around the world. In order to engineer coherent wavefronts and harness the high power densities, we need to develop X-ray deformable mirrors that can control the wavefront with high precision (< 5 nm-rms), can steer the beam at high speed (> 1 kHz) and be compatible with ultra-high vacuum environments. We show that deformable mirrors made on industry-grade silicon wafers, borrowing a technological platform developed for space X-ray telescopes, could potentially be used for synchrotron applications, with residual figure error of about 10 nm-rms that can be actuated to cause 100 nm PV local deformation and operation at frequencies up to 10 kHz. We also show that we can use machine learning techniques to improve their performance in operation, reducing the effects of drift and hysteresis, and make the device easier to calibrate periodically. We discuss future next steps such as stress compensation, fine substrate figuring and integrating electronics that would make them ready for use in experimental endstations at synchrotron beamlines.

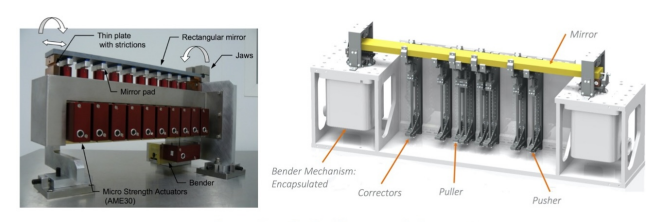
Keywords: Adaptive Optics, X-ray Optics, Metrology, Machine Learning, Neural Networks

1. INTRODUCTION

Synchrotron radiation and X-ray free-electron lasers have revolutionized atomic-scale material studies, demanding increasingly precise optical control. As light sources evolve toward higher brightness and coherence, adaptive X-ray optics have become essential for maintaining wavefront quality from source to sample, ^{1,2} and for demonstrating near diffraction-limited focusing performances. For next-generation synchrotron sources, such as the upgrades of the Advanced Light Source (ALS) and Advanced Photon Source (APS), wavefront preservation has become paramount. Wave optic simulations have established the range of correctable wavefront errors from heat load deformations, ⁴ and all new ALS beamlines will feature deformable mirrors to compensate for residual wavefront errors.

X-ray deformable mirrors fall into three main categories (Figure 1). Mechanical deformable mirrors^{5,6} expand the concepts of mechanical benders to sub-apertures of the mirror. Those mirrors are generally limited by mechanical complexity, the limited number of subapertures, their precision and their sensitivity to thermal drift. Thermal mirrors^{7,8} rely on an array of resistive elements to locally heat an actively cooled mirror to heat bumps on the surface of the mirror, generally used even out the heat loads caused by the incident X-ray beam, but that can be used to shape the wavefront, albeit with limited spatial resolution and low actuation speed. Piezoelectric bimorph mirrors^{9–11} rely on a piezoelectric material (generally Lead Zirconate Titanate (PZT)) that is glued on the mirror and that contracts when a voltage is applied, causing a strain on the mirror and a local deformation of the surface. Significant advancements in materials have expanded their capabilities, from glue-free designs for

^{*}Corresponding author. Email: awojdyla@lbl.gov



mechanical deformable mirrors (left: SOLEIL light source; right: ALBA)





Thermal mirror (developed at SLAC/ measurements at APS)





bimorph deformable mirrors (left: at Diamond Light Source; right: at NSLS-II)

Figure 1. Various deformable mirror technologies for X-ray synchrotron applications.

high-vacuum soft X-ray (SXR) applications 12 to monolithic lithium niobate-based mirrors with sub-nanometer stability. 13

Deformable mirrors impart a wavefront modification $\Delta \phi$ upon reflection at a grazing angle θ by locally modifying the height of the surface Δh , following:

$$\Delta \phi = 2 \times \frac{2\pi}{\lambda} \frac{\Delta h}{\sin \theta} \tag{1}$$

where λ is the wavelength. For typical soft X-ray applications, for 1 keV photon energy (corresponding to wavelength of 1.24 nm), at a grazing angle of θ =20 mrad, the control over the height needs to be in the order of $\Delta h = \lambda/(2 \times 14 \sin \theta) = 2.2$ nm-rms to achieve diffraction limited performance (Marechal criterion, $\lambda/14$ wavefront error).

To achieve this level of control, deformable mirrors often need to be paired with measurements and feedback, to actuate the surface and compensate for drift and hysteresis. This is generally done with interferometers in the visible range ^{14,15} which are cumbersome, or at wavelength using X-ray wavefront sensors, ^{16–18} which are generally invasive and cannot monitor the surface of the beam continually. While non-invasive X-ray wavefront sensors have been demonstrated, ¹⁹ those may not be readily integrated into experimental endstations, and techniques relying on machine learning have been developed ²⁰ to compensate for drift and hysteresis, and demonstrated reliable open-loop operations of piezo-electric bimorph mirrors ²¹ after initial calibration.

Beyond wavefront correction, bimorph mirrors could be used to steer X-ray beams at high speed, since piezoelectric devices can be run at ultrasonic speeds, by modifying the surface instead of moving the whole substrate. The ability to steer an X-ray beam is limited by the inertial speed limit²² of mirror holders (typically 100 Hz), often reducing beam scanning capabilities, which become crucial in the presence of high-brightness, nano-focused beams that can incur radiation damages to the samples. In some cases, radiation damage may be the point such as in the case of direct X-ray beam writing,²³ but the steering speeds are orders of magnitude below what e-beam lithography is capable of. Another use of fast beam steering is coherence engineering²⁴ or coherence busting,²⁵ but the speed or level of control device currently available is still quite limited. New ways

to steer the beam such as MEMS²⁶ or surface acoustic waves²⁷ could allow for faster scanning speed, but they rely on Bragg diffraction and do not work in the soft X-ray regime.

2. THIN ADAPTIVE OPTICS

Recent developments in space X-ray astronomy have demonstrated that thin-film PZT could be deposited on a curved substrate^{28,29} together with signal routing that allows addressing a large number of actuators (Figure 2) The goal of dense actuation is to correct residual slope error from manufacturing of the silicon shell substrates below 1 arcsec-rms (5 μ rad), so they can be used in space based on a Wolter-I telescope design.

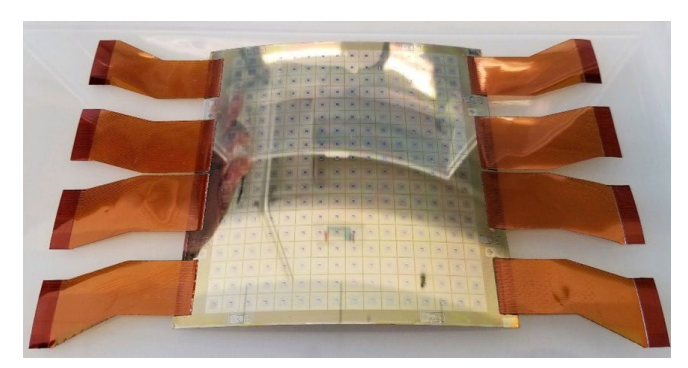


Figure 2. Example of adjustable X-ray mirror for space X-ray applications with 288 piezoelectric actuators arranged in 18 rows and 16 columns on a curved substrate shown with bonded anisotropic conductive film (ACF) cables, reprinted from Tendulkar.²⁹

The actuation of these devices has demonstrated a precision ($\tilde{1}$ nm) and a dynamic range ($\tilde{1}$ μ -PV)³⁰ comparable to bimorph mirrors commercially available for synchrotron based on thick (10 mm) substrates, but with much lower operating voltages (10 V vs. 500 V). Given the thickness of thin-film of PZT, actuation speed can in principle reach 10 kHz, much faster than the typical $\tilde{1}$ s actuation time¹⁵ for typical synchrotron piezoelectric bimorphs. Finally, the ability to have an arbitrary number of channels and to route the signals using an anisotropic conductive film (ACF) would help increase the precision and spatial resolution of wavefront correction, while making the mounting of the device easier.

Adapting this technological platform to synchrotron applications is not without challenges. First, the growth of the thin-film of PZT at high temperature creates a residual stress that significantly bends the substrate, though mitigation schemes using stress compensations layer are currently being developed. Second, the thinness of the substrate makes them sensitive to gravity sag and the mounting scheme, unsuitable for operation under high heatload and generally more sensitive to drift and hysteresis, non-idealities that could potentially be remediated with an appropriate controls scheme based on machine learning.

We have manufactured and characterized a first round of thin adaptive optics specifically designed for synchrotron applications in order to better understand current limitations and integration challenges, and to improve on the existing technology.

2.1 Design of thin adaptive optics

We have designed a batch of six Thin Adaptive Optics (TAO) device on a single wafer, to experiment with various mirror length and actuator densities (Figure 3). The substrate is a standard industry-grade 6 in. (152.4 mm), 500 μ m thick circular wafer, coated with silicon oxide for insulation, a 150 nm thick layer of platinum for the bottom electrode (with titanium adhesion layers), a 2 μ m-thick PZT thin-film and a patterned titanium electrode layer (additional details are available in a companion proceeding).

2.2 Manufacturing of thin adaptive optics

The TAO devices were manufactured at the Millennium Science Complex at Penn State University. The fabrication steps are detailed in a companion conference proceeding. After the deposition of the various layers, the wafer was cleaved into six segments to yield six deformable mirrors (Figure 4).

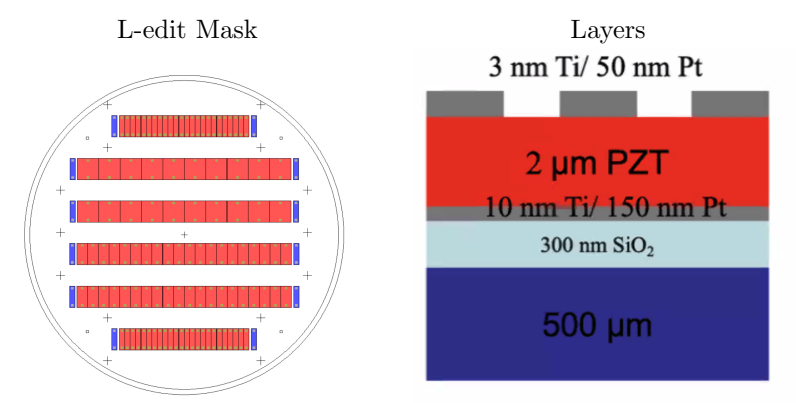


Figure 3. Design of thin adaptive optics. Left: Wafer layout of the six Thin Adaptive Optics (TAO) device. Right: cross-section of the Thin Adaptive Optics.

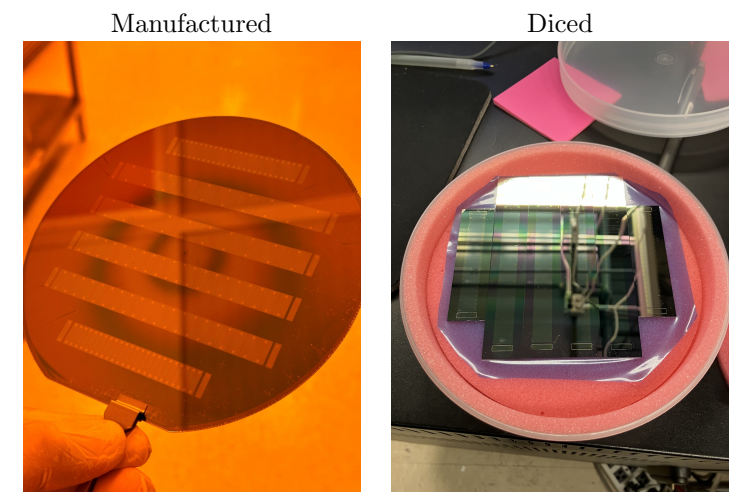


Figure 4. Manufacturing of thin adaptive optics. Left: after the deposition of the various layers. Right: after cleaving the wafer into six operational segments.

2.3 Morphological and electrical characterization of thin adaptive optics

During the fabrication, the morphology of the PZT layer was characterized to enable that the (001) orientation had been successfully promoted during the growth. We also performed the electrical characterization of the segment to assess actuation performance and operational bandwidth (Figure 5). The RC frequency of the device is about 13 kHz.

3. CHARACTERIZATION OF THIN ADAPTIVE OPTICS

3.1 Substrate characterization

We performed an initial measurement of the surface of TAO segment 3A (80 mm \times 20 mm, with 24 cells, each measuring 10 mm \times 2.5 mm) with a Fizeau interferometer at Lawrence Berkeley National Laboratory (Figure 6) and we found that the segment has an intrinsic radius of curvature of 50 m (typical flat X-ray mirrors have residual radius of curvature above 10 km), caused primarily by the internal stress in PZT layer. With the radius of curvature removed, the residual height error in the tangential direction is about 100 nm-PV, typical of industrial-grade silicon wafer.

3.2 Characterization of the active device

We performed the characterization of the active device at the University of Iowa. We mounted TAO segment 3A (80 mm \times 20 mm, with 24 cells, each measuring 10 mm \times 2.5 mm) on a solder breadboard using kapton tape,

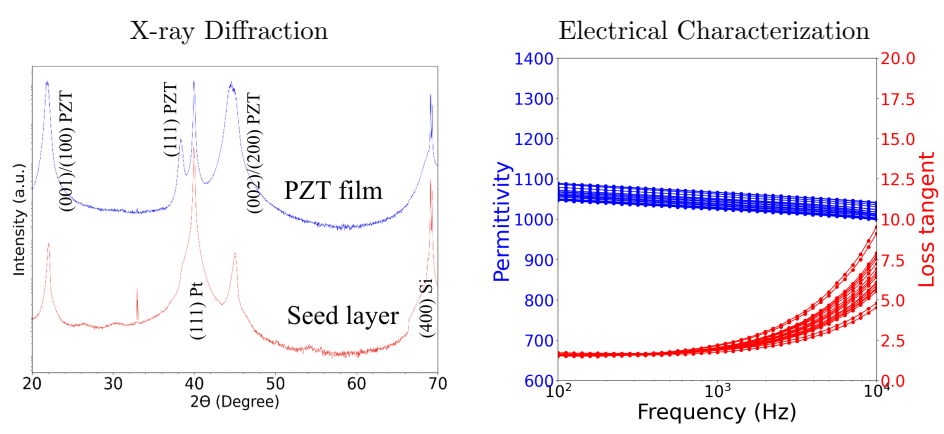


Figure 5. Morphological and electrical characterization of thin adaptive optics. Left: XRD characterization of thin-film morphology. Right: Electrical characterization of type II segments (10 mm× 5 mm electrode).

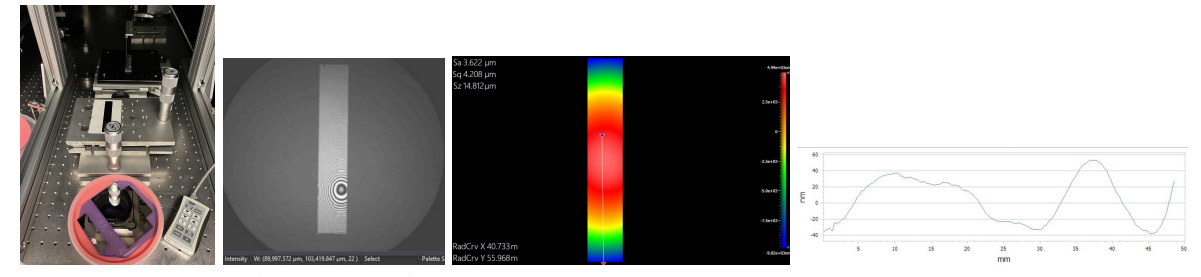


Figure 6. Measurement of TAO segment 3A without actuation. Far left: measurement setup with a Fizeau interferometer. Center left: raw measurement from the Fizeau interferometer. Center right: surface height error, showing a radius of curvature of about 50 m (caused by internal stress in PZT layer). Far right: line cut along the tangential direction of the mirror segment with power removed showing a 100 nm-PV residual figure error.

and we wire bonded the individual channels to the breadboard, in order to provide an electrical interface for the voltage controller (Figure 7). Some of the leads were damaged during transportation, and a few channel couldn't be actuated. We also conducted another measurement campaign on another segment, segment 2A (115 mm \times 20 mm with 20 cells of size 10 mm \times 5 mm) where all the channels could be actuated.



Figure 7. Experimental setup for the measurement of thin adaptive optics segment 3A at the University of Iowa.

The Fizeau interferometer was a 4D Technologies Accufiz. We measured the device with all the channels at 0 V, to measure the baseline shape of the mirror and subtract it from the subsequent measurements. Given the mounting of the mirror, we measured the face of the substrate with the electrode, though the X-ray reflective surface should be the backside of the substrate. We then actuated the channel individually using a Galil RIO-47142 controller that provides 10 V outputs (Figure 8). The measurements indicate that channels have a typical sensitivity of about 5 nm/V peak-to-valley for 5 mm \times 10 mm electrodes. Note that negative voltages do not reverse the direction of the height change, and should generally be avoided so as not to depolarize the PZT.

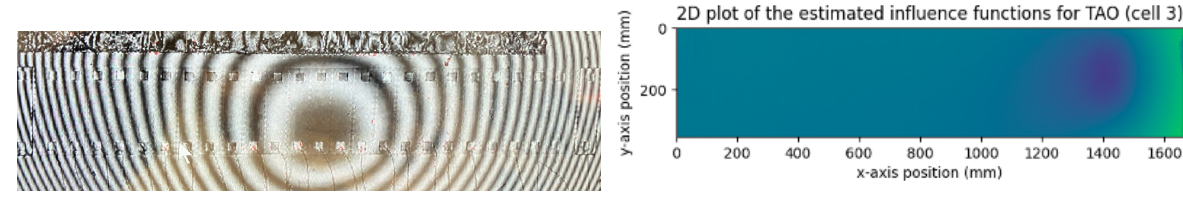


Figure 8. Fizeau interferometry measurement of thin adaptive optics (segment 3A). Left: raw interferogram showing the electrodes. Right: sample measurement after the actuation of the rightmost actuators (the colorbar goes from -20 nm to +30 nm).

1600

Further details about metrology of the device can be found in the companion conference proceedings "Metrology of thin adaptive optics for X-ray beamlines", with complete characterization of the influence function, linearity, hysteresis and drift, and complete details about the experimental conditions.

In the rest of the paper, we are interested in using machine learning models characterize the device using random measurements, in order to simplify the calibration and integrate hysteresis and drift directly into the model in order to compensate for those effects.

3.3 Active device characterization using Machine Learning

For active characterization of the TAO device, we address two key tasks using machine learning (ML) models: influence function prediction and wavefront reconstruction. For the first task, we developed a ML model, referred to as the predictor, which learns the relationship between randomly applied voltages and the resulting mirror shapes (also termed "wavefront") of the TAO device. This enables accurate prediction of the influence function by systematically applying voltage to each actuator. For the second task, a complementary ML model, termed the generator, is used to infer the voltage pattern required to produce a given mirror shape. An overview of the proposed framework is shown in Figure 9.

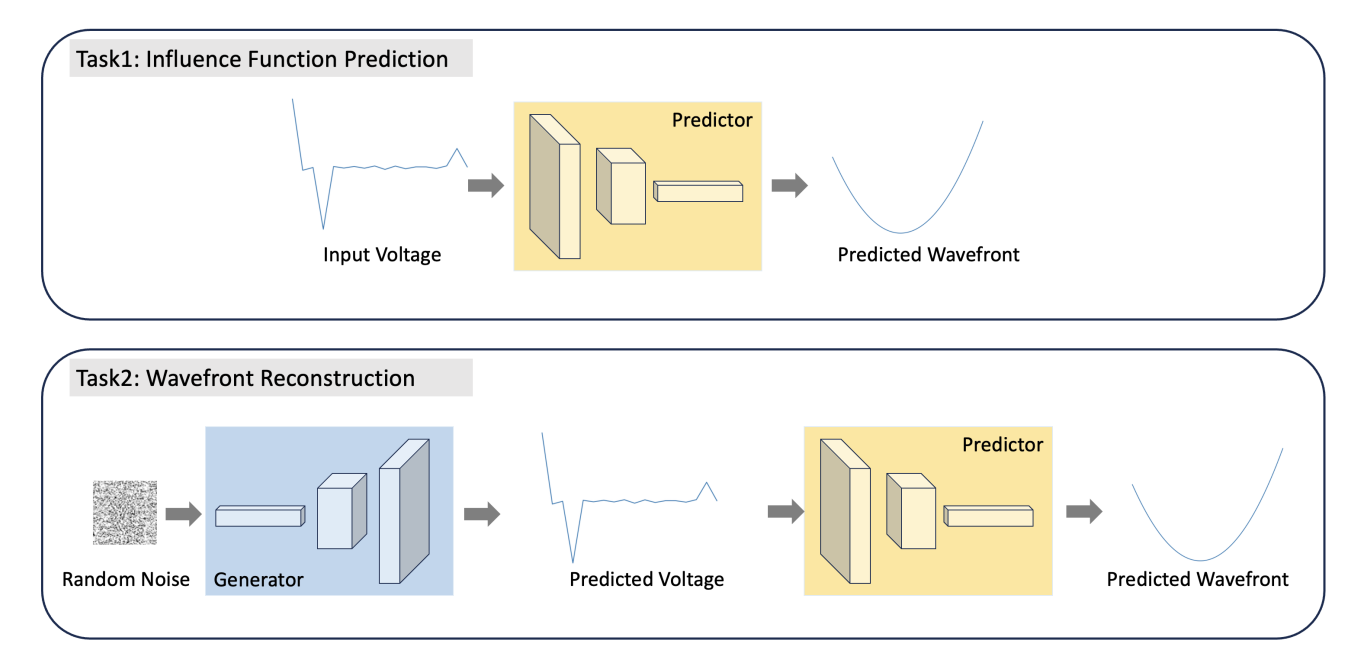


Figure 9. Overview of the machine learning-based architecture. The top section illustrates the influence function prediction pipeline, while the bottom section depicts the mirror shape reconstruction pipeline.

3.3.1 Data Collection

The training data consists of pairs of input voltages x and their corresponding output mirror shape y, obtained by applying known voltages to the TAO device and measuring the resulting mirror shape. These (x, y) pairs form the foundation for training our machine learning models. We conduct two types of experiments to get training data: simulated data and experimental data.

To obtain simulated data, we perform an influence function extraction experiment, where 10 V is applied to each actuator cell individually and the resulting wavefront is recorded. This provides a systematic understanding of the effect of each actuator and captures the influence function for every channel. Since the influence functions are collected directly, we simulate training data by applying random voltage combinations to these measured functions to compute the corresponding mirror shapes.

For experimental data, we perform a random voltage experiment, in which random voltages are simultaneously applied to all actuator cells, and the resulting mirror shapes are measured. This dataset inherently captures noise and potential temporal dependencies between samples. By introducing a broader range of input conditions, this method enables the model to learn complex, nonlinear relationships between voltages and mirror shapes. Unlike the simulation-based approach, this method directly yields usable training pairs without requiring additional modeling or pre-processing.

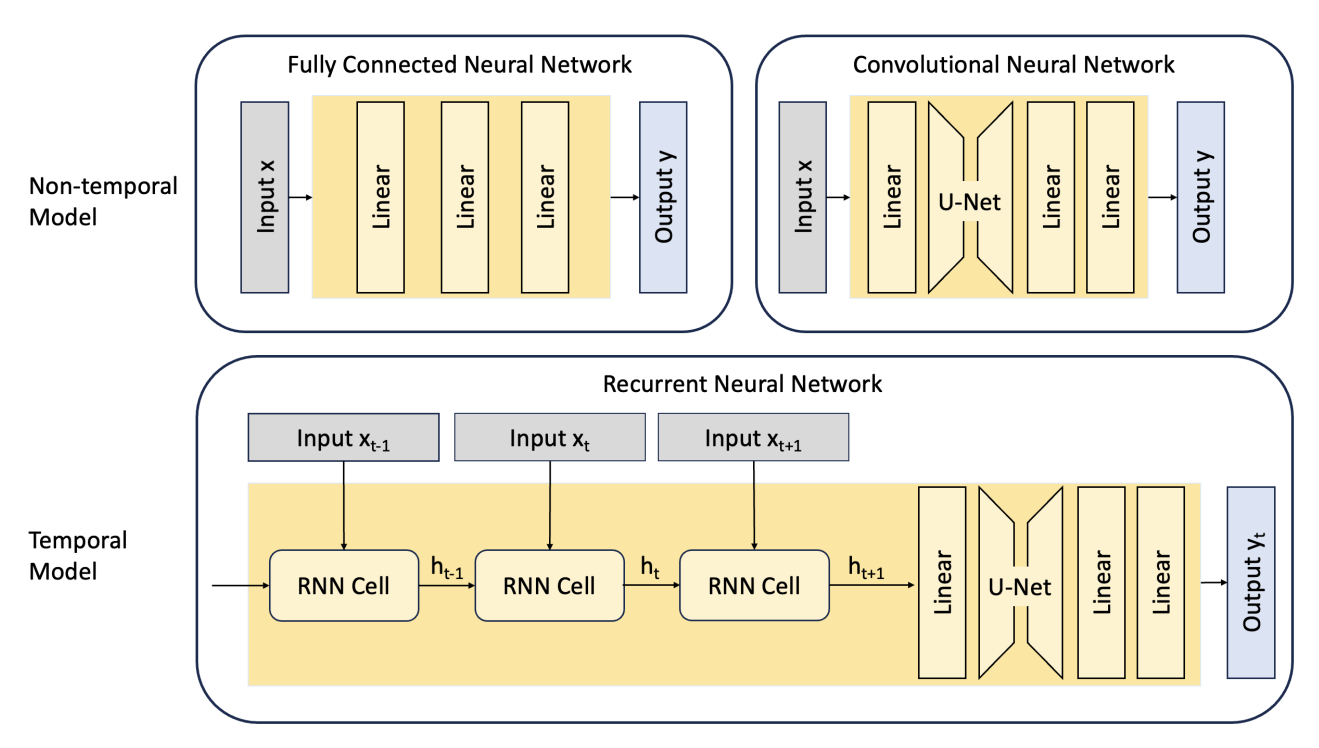


Figure 10. Architectures of the predictor. The upper panel illustrates non-temporal models, including a fully connected neural network and a convolutional neural network. The lower panel shows a temporal model based on a recurrent neural network.

3.3.2 Influence Function Prediction

In the context of adaptive optics, the relationship between the input voltage x and the output mirror shapes y is governed by the influence function A, represented by the equation:

$$Ax = y \tag{2}$$

We use a predictor P to learn the influence function A from the training data by minimizing the mean squared error (MSE) between the predicted wavefront P(x) and the actual wavefront y:

$$min \left\| P(x) - y \right\|^2 \tag{3}$$

The predictor P is trained to map the input voltage x to the output wavefront y, effectively learning the influence function A. This step involves optimizing the predictor's parameters to accurately predict the mirror shapes from the input voltages, thereby capturing the underlying relationship modeled by A.

The architecture of the predictor is illustrated in Figure 10. We explore three types of models. The first is a fully connected neural network (FCNN), which is suitable for handling ideal, simulated data where temporal dependencies are minimal. The second is a convolutional neural network (CNN) named U-Net, 31 which is better suited for processing experimental data due to its ability to capture spatial correlations. The third is a recurrent neural network (RNN), 32 which explicitly accounts for temporal dependencies by considering sequences of inputs over time. 33 This is particularly useful in cases where the predicted wavefront at current time step t depends on the mirror's previous states—such as when the mirror shape has not fully recovered from previously applied voltages. In the experimental results section, we apply these three types of models to different datasets based on their characteristics.

In temporal models, predicting the current wavefront y_t at time step t requires not only the current voltage x_t but also contextual information from previous and future voltage inputs applied to the mirror. To capture these temporal dependencies, we construct a time-series dataset where the model input is defined as $X_t = (x_{t-m}, ..., x_{t-1}, x_t, x_{t+1}, ..., x_{t+n})$, representing a window of length m+n+1. In our experiments, we set m=n=2. The predictor is then trained by minimizing the following loss function:

$$\min \|P(X_t) - y_t\|^2 \tag{4}$$

After training the predictor network to learn the mapping from input voltages to output mirror shapes, we estimate the influence function by sequentially applying 1 V to each actuator cell, recording the corresponding mirror shapes, and aggregating the results across all channels to construct the predicted influence function.

3.3.3 Mirror shape reconstruction

In addition to learning the forward mapping from input voltages to resulting mirror shapes, we also address the inverse problem: predicting the voltage pattern required to generate a given target mirror shape. To do this, we employ a generator G that takes a random noise vector as input and outputs a voltage G(noise). The generator is trained by minimizing the mean squared error between the predicted wavefront P(G(noise)) and the target wavefront y:

$$\min \|P(G(\text{noise})) - y\|^2 \tag{5}$$

This training process encourages the generator to produce voltage inputs that, when passed through the predictor P, yield mirror shapes closely matching the desired target. Given that the generator's goal is to output voltage patterns, a simple fully connected neural network—similar to the predictor architecture shown in Figure 10—is sufficient.

4. RESULTS

4.1 Data Collection

As mentioned in Section 3.3.1, we collect both simulated and experimental data to train machine learning models. The details of the two methods are illustrated as follows.

Simulated Data. We begin by applying a voltage of 10 V to each cell of the TAO device and collecting the resulting wavefront data. The raw influence functions extracted from this process are illustrated in Figure 11(a)(b).

The raw data contains noise, necessitating post-processing steps to ensure data quality and accuracy. The processed influence functions are illustrated in Figure 11(c)(d). Specifically, the post-processing steps include:

• Interpolation: Smooths the data by filling in gaps and generating a continuous representation that more accurately reflects the wavefront shapes.

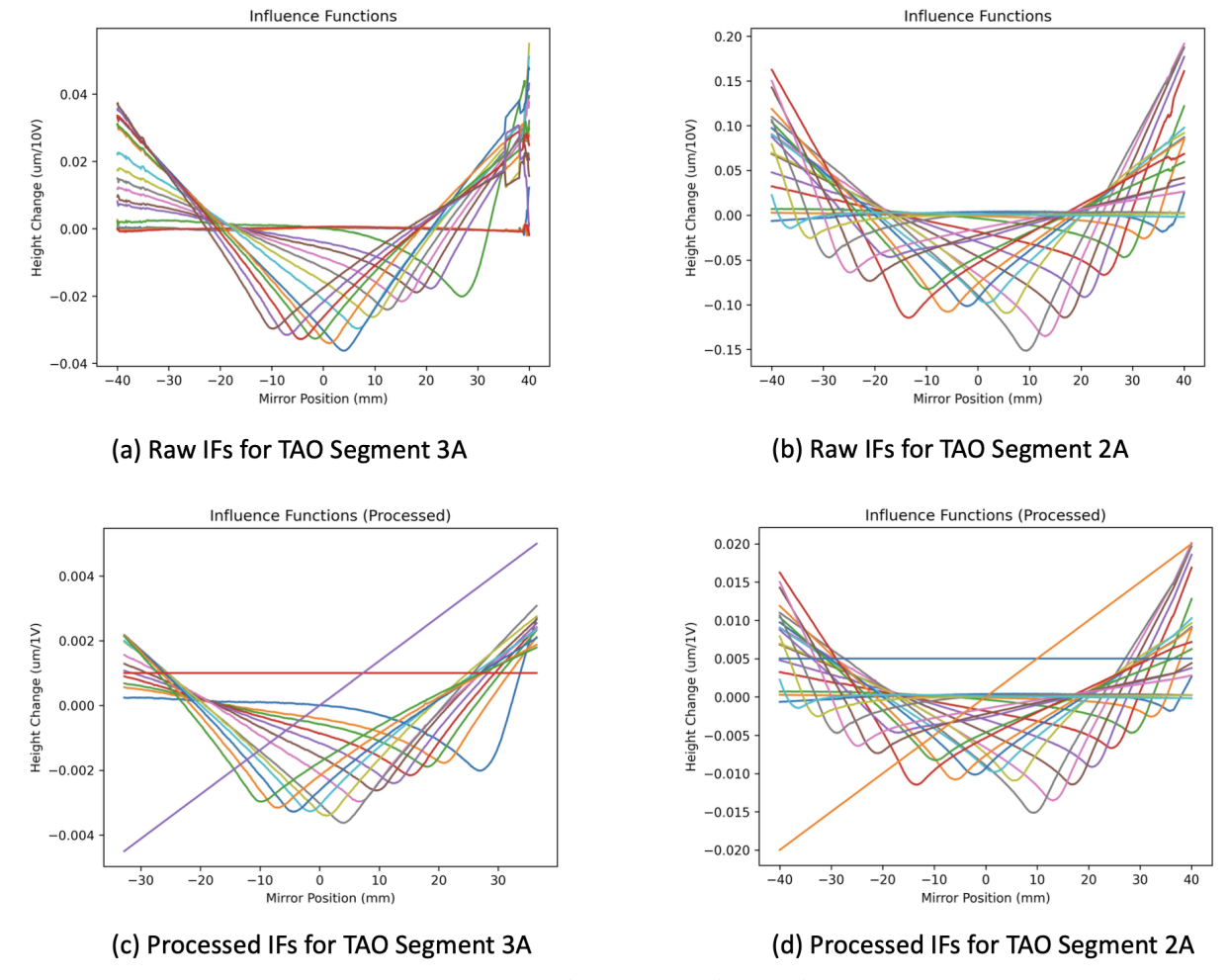


Figure 11. Raw and processed influence functions for TAO segment 3A and 2A. Note that we added a constant and linear term in the processed influence function to account for piston and tilt terms that are solid body motion in our subsequent mirror shape optimization

- Cropping: Removes irrelevant regions from the dataset to focus on the area of interest, reducing computational load and eliminating noise from extraneous areas.
- Defective Cell Removal: Excludes identified defective cells that could introduce noise or artifacts, ensuring the data used for analysis is clean and reliable.
- Line Addition: Adds a constant and linear term to the processed influence function to remove solid body motion in our mirror shape optimizations.
- Height Normalization: Since each cell is actuated with 10 V, the measured height changes are divided by 10 to obtain the normalized influence function per volt.

After obtaining the processed influence functions, we generate random voltages for each actuator cell, with values uniformly sampled from the range of 0 to 10 V. These voltages simulate various operational conditions that the TAO device might encounter. For each random voltage vector, the corresponding wavefront is computed using the linear superposition principle, as defined in Equation 2, where the influence function serves as the basis for reconstructing the optical response.

This procedure enables the construction of a comprehensive simulated dataset that captures the relationship between diverse voltage configurations and their resulting mirror shapes. By systematically varying the input voltages, we ensure a broad coverage of possible system states, which is essential for training robust machine learning models.

The simulated dataset consists of 5000 training pairs, each comprising a randomly generated voltage vector and its corresponding computed wavefront. Simulated mirror shapes for TAO segments 3A and 2A are shown in Figure 12(a)(b). This dataset provides a noise-free, idealized foundation for training and evaluating models that learn the forward and inverse mappings between voltages and mirror shapes.

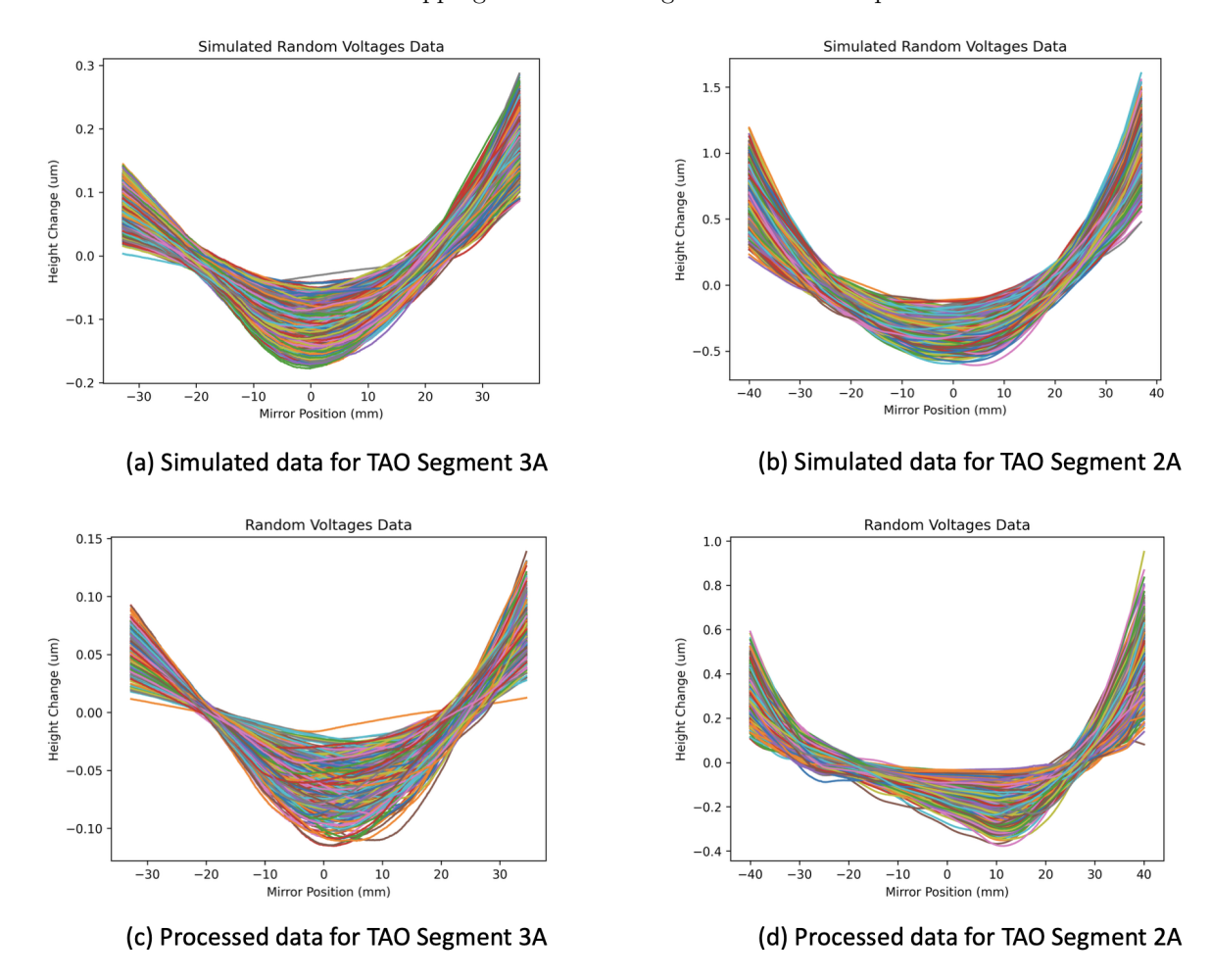


Figure 12. Simulated and experimental random voltages data.

Experimental Data. In this method, we collect the experimental data by applying random voltages to the TAO device and recording the resulting mirror shapes. Each voltage vector is composed of independently selected values across all actuator cells, introducing a wide variety of input conditions that help the system explore a broad range of wavefront responses. This approach provides a rich and diverse dataset, enabling machine learning models to learn the complex and potentially nonlinear mapping between input voltages and the resulting mirror shapes.

We apply similar data processing steps as described in Method 1, including interpolation, cropping, and defective cell removal. However, unlike Method 1, piston and tilt removal addition and height normalization are not necessary in this case. The processed wavefront data obtained from these experiments is illustrated in Figure 12(c)(d). These measurements form the foundation for training models to predict the influence function directly from real-world experimental data, offering a more accurate depiction of system behavior under practical usage.

Meanwhile, we also intend to collect time-series data, where random voltage inputs are applied sequentially over multiple time steps to the same device. This setup allows us to observe how the mirror's response evolves over time and to capture potential temporal dependencies—especially in scenarios where the mirror's surface does not fully recover to its resting shape between consecutive voltage inputs. This sequential data will be used to develop and train temporal models, such as recurrent neural networks (RNNs), which are well-suited for capturing time-dependent dynamics and improving the accuracy and robustness of wavefront prediction in dynamic operational settings.

4.2 Influence Function Prediction

We apply machine learning techniques to reconstruct the influence function for both the simulated and experimental data. We first learn the mapping between random voltages and corresponding mirror shapes. After that, we systematically apply a voltage of 1 V to each cell in the TAO device and collect the corresponding mirror shapes. This process is repeated for each cell individually. By aggregating the mirror shapes obtained for each cell, we can reconstruct the overall influence function.

The predicted influence functions for simulated data are shown in Figure 13. The figure demonstrates that the predicted influence function is accurate and aligns well with the ground truth values, indicating the effectiveness of our approach in capturing the true relationship between input voltages and resulting wavefronts. Since the simulated data is ideal, a simple network—such as the fully connected neural network shown in Figure 10—is sufficient for accurate prediction.

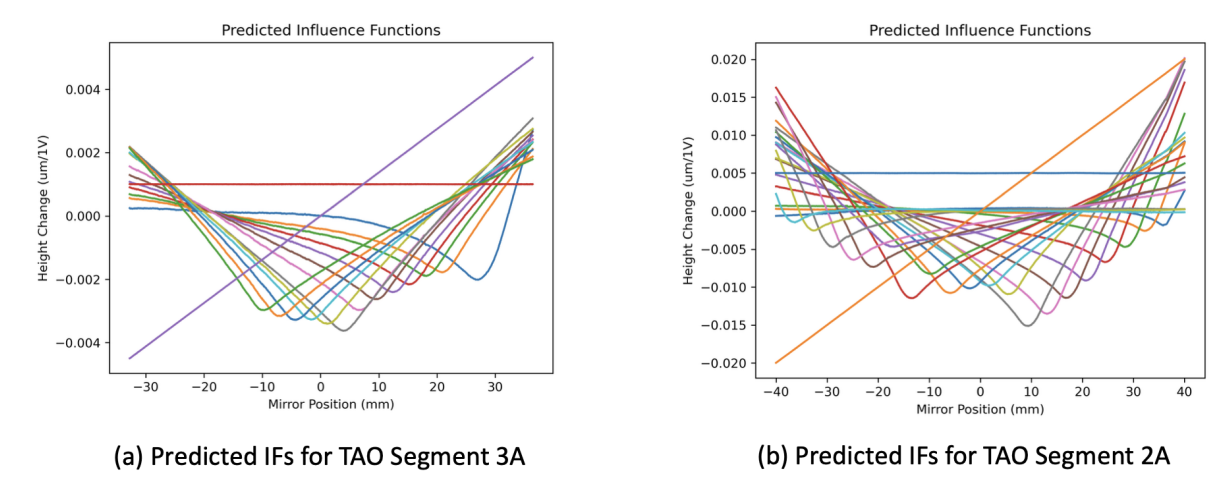


Figure 13. Predicted influence functions on simulated data.

For experimental data, we apply random voltages to TAO segment 3A to collect the corresponding mirror shapes and use the convolutional neural network shown in Figure 10 to train the predictor. Figure 14(a) illustrates the predicted influence function for segment 3A. This task is more challenging than with simulated data due to the presence of measurement noise and the fact that the relationship between input voltages and resulting mirror shapes is not strictly linear. Although the prediction does not exactly match the extracted influence function, it aligns well with the expected behavior and likely reflects the true system response.

To further investigate temporal dependencies, we collected time-series data for segment 2A, where the wave-front shape depends on the mirror's previous state, which may not fully recover between time steps. We employ the recurrent neural network shown in Figure 10 as the predictor, as non-temporal models fail to produce reasonable results in this setting. This constitutes the most challenging prediction task, with results presented in Figure 14(b). Overall, the results are reasonable and demonstrate the effectiveness of our approach in capturing the complex, nonlinear dynamics between voltages and mirror shapes, highlighting promising directions for future research.

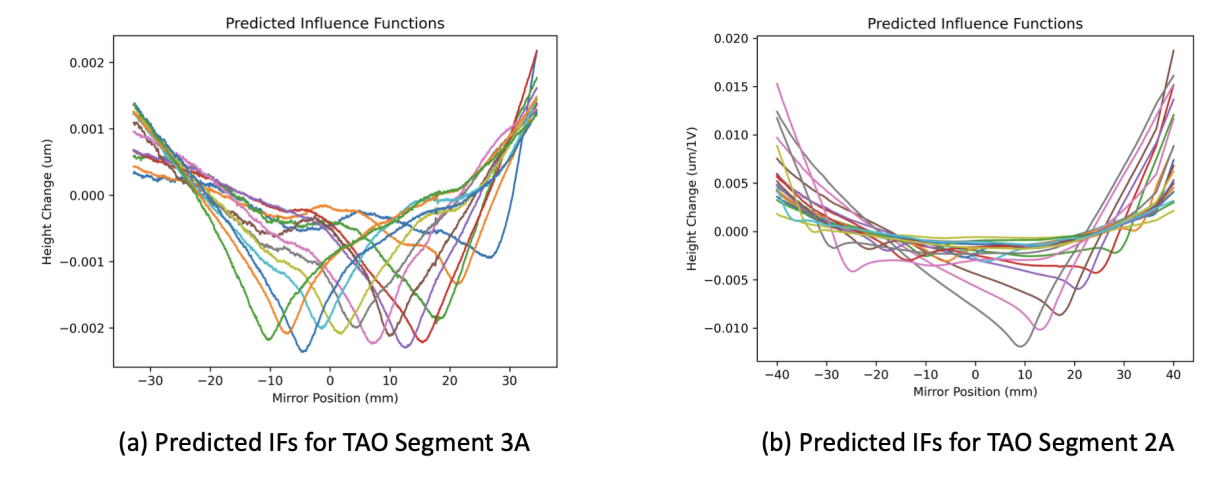


Figure 14. Predicted influence functions on experimental data.

Although the predicted influence functions are not identical to the extracted ones shown in Figure 11, we believe the machine learning-predicted influence functions better reflect real-world behavior. We validate this through a wavefront prediction test. Specifically, we select a random voltage sample from the dataset and feed it into the trained machine learning model to obtain the predicted wavefront, labeled as "ML Prediction" (blue curve in Figure 15(a)). The actual measured mirror shape under the same voltage is shown as "Target" (orange curve), while the expected shape derived by multiplying the voltage with the extracted influence functions (Figure 11) is labeled as "Predicted by IFs" (green curve). As shown in Figure 15(a), the "ML Prediction" closely matches the "Target", whereas the "Predicted by IFs" differs significantly. This suggests that the influence functions observed in real-world conditions deviate from those extracted under ideal settings. A similar observation can be made for segment 2A, as illustrated in Figure 15(b).

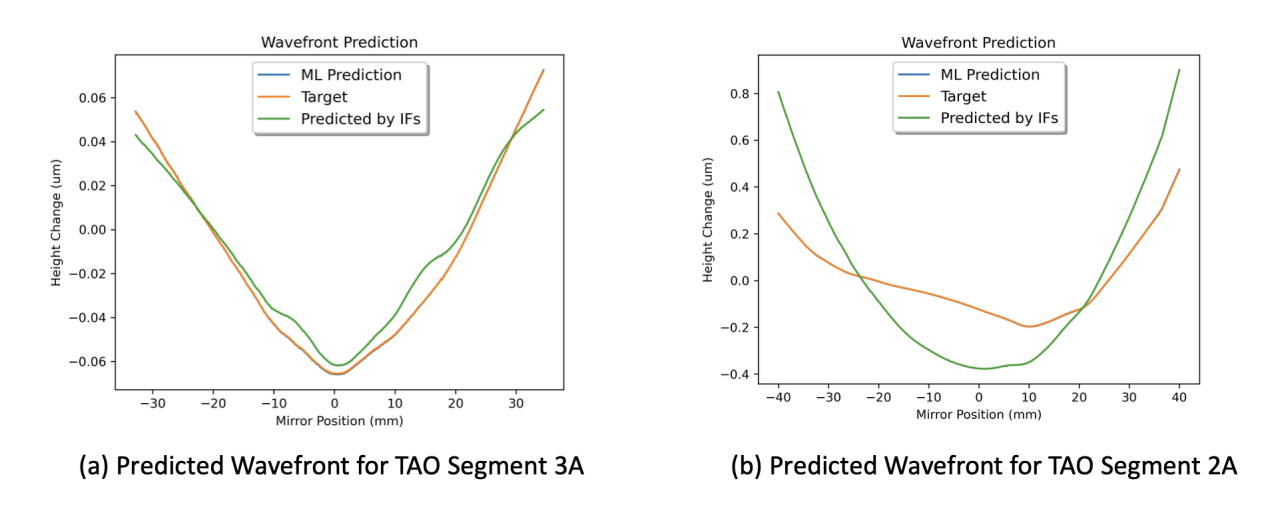


Figure 15. Comparison of mirror shape predictions for a selected voltage input using experimental data.

4.3 Mirror shape reconstruction

Next, we aim to predict the voltages required to achieve a predefined target wavefront. Once the voltages are predicted, we use the previously trained predictor model to get the corresponding mirror shapes. These reconstructed mirror shapes are then compared to the target mirror shapes to evaluate prediction accuracy.

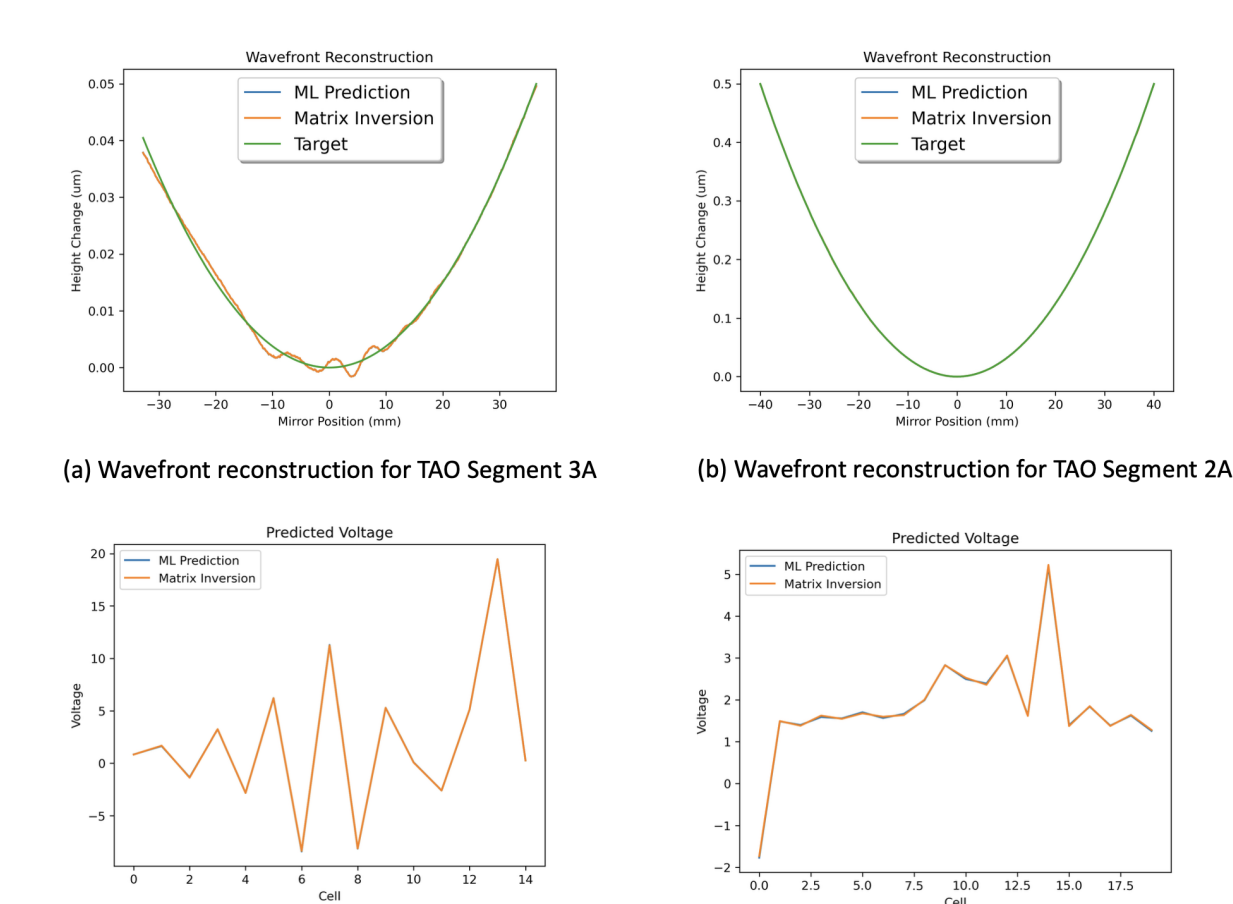


Figure 16. Mirror shapes reconstruction result for network trained on simulated data.

(c) Predicted voltage for TAO Segment 3A

For this experiment, we defined a specific target wavefront and predicted the corresponding voltages using both traditional matrix inversion techniques and a deep learning-based approach. For the matrix inversion method, the predicted voltage x is calculated by:

$$x = A^{-1}y \tag{6}$$

(d) Predicted voltage for TAO Segment 2A

For the machine learning approach, the voltage is predicted using a neural network model as described in Equation 5. Once the predicted voltages are obtained, we use the influence function to reconstruct the mirror shapes and compare them with the target mirror shapes.

We performed mirror shape reconstruction experiments for both TAO segment 3A and segment 2A. A target wavefront was defined, as illustrated by the green curve in Figure 16(a), and the generator model was used to predict the voltages required to reproduce this mirror shape. As shown in Figures 16(c) and (d), the predicted voltages from both the traditional matrix inversion and the deep learning-based methods are comparable, demonstrating the robustness and reliability of the machine learning approach.

Figures 16(a) and (b) present the comparison between the reconstructed and target mirror shape for both methods. These results confirm that the machine learning model is capable of accurately predicting the voltages necessary to achieve the desired wavefront configurations. Notably, the reconstruction performance is better for segment 2A, which has 20 actuator cells compared to 13 in segment 3A, allowing for finer resolution and more precise control of the wavefront shape.

We then validate the performance of our approach by applying the predicted voltages-obtained from the trained models-to the physical TAO segment 3A device. This step is critical for assessing the real-world ap-

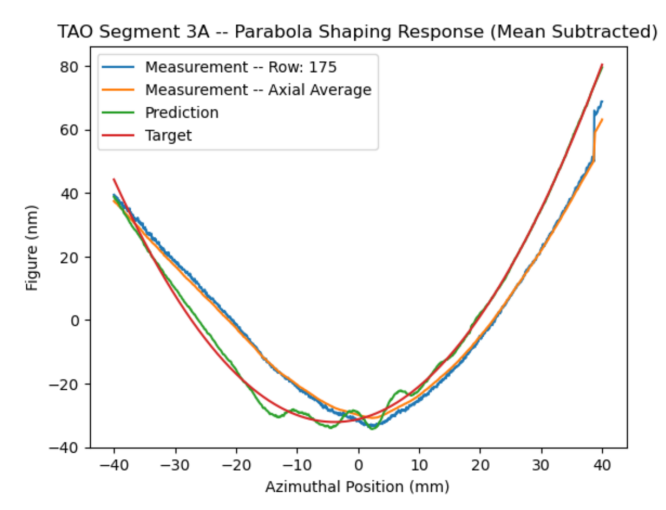


Figure 17. Comparison of measured mirror shape and target.

plicability of the machine learning-based predictions. After applying the voltages to the deformable mirror, we measure the resulting mirror surface shape. This measurement provides a direct comparison between the model-generated predictions and the actual physical response of the system.

The experimental results are shown in Figure 17. Visually and quantitatively, the reconstructed wavefront closely aligns with both the target wavefront and the predicted wavefront from the machine learning model, confirming the accuracy and robustness of our data-driven approach. Despite this strong agreement, a slight horizontal shift is observed in the measured wavefront. Nevertheless, the overall fidelity of the reconstructed wavefront demonstrates the practical viability of the proposed method for real-time adaptive optics control.

This validation experiment underscores the importance of bridging simulation with experimental execution and reinforces the potential of machine learning models to not only predict system behavior but also to drive hardware in practical scenarios with high accuracy.

4.4 Dynamic characterization: measurement of actuation speed

We measured the TAO segment 3A using a laser fiber interferometer (SmarAct Picoscale) to directly measure a local height change at speeds faster than allowed by a Fizeau interferometer. We measured height changes of about 50 nm at 10 Hz (Figure 18, left). The inadequate mounting (the TAO segment laying flat on a mount) didn't allow us to measure the device at higher speeds, though there was an audible noise emanating from the device at frequencies up to 10 kHz. The first natural frequency for a segment of length L=120 mm and thickness h=500 μ m in a cantilevered configuration¹¹ would be about:

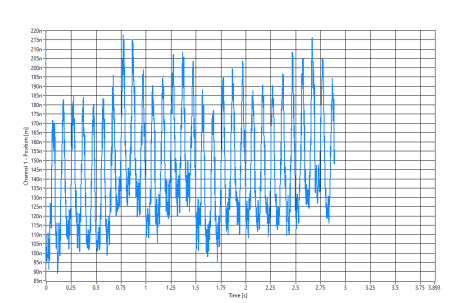
$$f = \frac{1.875^2}{4\pi} \frac{h}{L^2} \left(\frac{E}{3\rho}\right)^{1/2} = 50Hz$$

where E is Young's modulus and ρ is the density of silicon.

In order to perform measurement at high speed, we developed a deflection setup (described in the companion paper) where a laser beam shines of the device and the position of the spot is detected downstream. We were able to measure repeatable changes in the beam position after actuating all the channels to 10 V at rates up to 100 Hz (Figure 18, right), with a deflection of typically 2 μ rad which is consistent a 100 nm height change over 50 mm (half the mirror length).

Further investigation is needed to fully characterize the behavior of the TAO segments at frequencies up to 10 kHz to determine whether the device can reliably used at such speed.

Single-Cell Actuation at 10 Hz



All-Cells Actuation at 100 Hz

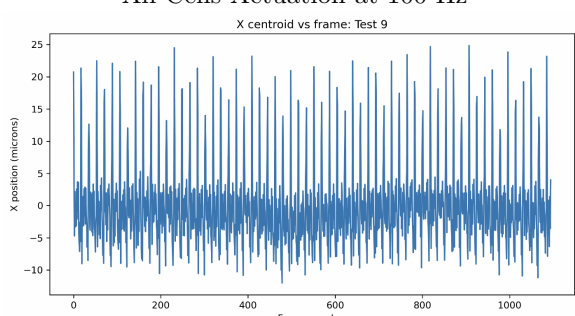


Figure 18. Dynamic characterization of thin adaptive optics. Left: at 10 Hz with 10 V drive voltage on the center cell measured with a fiber laser interferometer. Right: at 100 Hz with a drive voltage of 10 V on all the cells, measured by deflecting a laser beam on a camera.

5. CONCLUSION AND FUTURE DIRECTIONS

We have developed, manufactured and characterized a deformable mirror based on thin-film PZT deposited on a silicon wafer, borrowing from a technological platform initially developed for space X-ray telescopes, and demonstrated that the performances could make it a viable candidate for integration into synchrotron endstations, providing enough precision and dynamic range for coherent X-ray beams, and that we could leverage machine learning techniques to improve controls and reduce the effect of drift and hysteresis.

While the current device has known (and expected) limitations, they will be addressed in the next round of design. First, the bending caused by the stress in the PZT film can be compensated by adding a layer of silicon dioxide³⁴ to flatten the device. Second, the residual mirror figure error could be removed after a ion-beam figuring.³⁵ Third, a better routing of the signal can be achieved using anisotropic conductive film,²⁹ which would also allow increasing the number of actuators. Last, a better mechanical scheme will be designed to make measurement more robust at high-speed and perform characterization with X-ray beams.

ACKNOWLEDGMENTS

Xiaoya Chong and Antoine Islegen-Wojdyla are supported by an Early Career Award in the X-Ray Instrumentation Program, in the Science User Facility Division of the Office of Basic Energy Sciences of the U.S. Department of Energy, under Contract No. DE-AC02-05CH11231. K. Buffo acknowledges the support of the NASA FINESST grant (80NSSC23K1483) and funding from the Iowa Space Grant Consortium Graduate Student Fellowship. The authors would like to thank Phathakone Sanethavong from Lawrence Berkeley National Laboratory for his help with the wire bonding of the devices. The authors would also like to thank Samuel Hisel from University of Iowa for his help with fabricating mirror connection cables.

REFERENCES

- [1] Cocco, D., Cutler, G., del Rio, M. S., Rebuffi, L., Shi, X., and Yamauchi, K., "Wavefront preserving x-ray optics for synchrotron and free electron laser photon beam transport systems," *Physics Reports* **974**, 1–40 (8 2022).
- [2] Wojdyla, A. and Goldberg, K. A., "Wavefront preservation in soft x-ray beamlines for the advanced light source upgrade," *Synchrotron Radiation News* **34**, 21–26 (11 2021).
- [3] Mimura, H., Handa, S., Kimura, T., Yumoto, H., Yamakawa, D., Yokoyama, H., Matsuyama, S., Inagaki, K., Yamamura, K., Sano, Y., Tamasaku, K., Nishino, Y., Yabashi, M., Ishikawa, T., and Yamauchi, K., "Breaking the 10 nm barrier in hard-x-ray focusing," *Nature Physics* 6, 122–125 (2 2010).
- [4] Rio, M. S. D., Wojdyla, A., Goldberg, K. A., Cutler, G. D., Cocco, D., and Padmore, H. A., "Compensation of heat load deformations using adaptive optics for the als upgrade: A wave optics study," *Journal of Synchrotron Radiation* 27, 1141–1152 (2020).

- [5] Mercère, P., Idir, M., Dovillaire, G., Levecq, X., Bucourt, S., Escolano, L., and Sauvageot, P., "Hartmann wavefront sensor and adaptive x-ray optics developments for synchrotron applications," in [Adaptive X-Ray Optics], 7803, 780302, SPIE (8 2010).
- [6] Nicolas, J., Colldelram, C., Ruget, C., Ribó, L., Pedreira, P., de la Rubia, P., Martín-Nuño, C., Úbeda, D., and Tomàs, A., "Nanometer figure correction of x-ray mirrors using multiple spring actuators," 9965, 996503 (10 2016).
- [7] Cocco, D., Hardin, C., Morton, D., Lee, L., Ng, M. L., Zhang, L., Assoufid, L., Grizolli, W., Shi, X., Walko, D. A., Cutler, G., Goldberg, K. A., Wojdyla, A., Idir, M., Huang, L., and Dovillaire, G., "Adaptive shape control of wavefront-preserving x-ray mirrors with active cooling and heating," Optics Express 28, 19242 (2020).
- [8] Zhang, W., Gong, X., Lu, Q., Bai, Y., Song, Y., Zhang, Z., Chai, K., Li, A., and Liu, Q., "A hybrid surface shape control method for optimizing thermal deformation of fel reflection mirror," *Nuclear Instruments and Methods in Physics Research, Section A: Accelerators, Spectrometers, Detectors and Associated Equipment* 1062 (5 2024).
- [9] Susini, J., Labergerie, D. R., and Hignette, O., "R and d program on bimorph mirrors at the esrf," in [Optics for High-Brightness Synchrotron Radiation Beamlines II], Berman, L. E. and Arthur, J., eds., 2856, 130–144 (11 1996).
- [10] Sawhney, K., Alcock, S. G., and Signorato, R., "A novel adaptive bimorph focusing mirror and wavefront corrector with sub-nanometre dynamical figure control," in [*Proc. SPIE*], **7803**, 780303 (8 2010).
- [11] Goldberg, K. A. and Fleche, K. T. L., "Controlling cantilevered adaptive x-ray mirrors," *Journal of Syn*chrotron Radiation 31, 1161–1167 (9 2024).
- [12] Ichii, Y., Okada, H., Nakamori, H., Ueda, A., Yamaguchi, H., Matsuyama, S., and Yamauchi, K., "Development of a glue-free bimorph mirror for use in vacuum chambers," *Review of Scientific Instruments* **90**, 1–5 (2019).
- [13] Inoue, T., Nakabayashi, S., Uematsu, K., Tanaka, Y., Nakamori, H., Kohmura, Y., Yabashi, M., and Matsuyama, S., "Monolithic deformable mirror based on lithium niobate single crystal for high-resolution x-ray adaptive microscopy," *Optica* 11, 621 (5 2024).
- [14] Badami, V. G., Abruña, E., Huang, L., and Idir, M., "In situ metrology for adaptive x-ray optics with an absolute distance measuring sensor array," *Review of Scientific Instruments* **90**, 1–14 (2 2019).
- [15] Nistea, I.-T., Alcock, S. G., Foster, A., Badami, V., Signorato, R., and Fusco, M., "Picometre-level surface control of a closed-loop, adaptive x-ray mirror with integrated real-time interferometric feedback," *Journal* of Synchrotron Radiation 32, 133–144 (1 2025).
- [16] Grizolli, W. C., Shi, X., Assoufid, L., Kolodziej, T., and Shvyd'ko, Y., "Single-grating talbot imaging for wavefront sensing and x-ray metrology," in [Advances in Metrology for X-Ray and EUV Optics VII], Assoufid, L., Ohashi, H., and Asundi, A. K., eds., 1, SPIE (9 2017).
- [17] Wojdyla, A., Bryant, D., Chao, W., Assoufid, L., Cocco, D., Idir, M., and Goldberg, K. A., "Design and demonstration of tunable soft x-ray lateral shearing and hartmann wavefront sensors," in [Advances in X-Ray/EUV Optics and Components XIII], 1076003, 3 (2018).
- [18] de La Rochefoucauld, O., Dovillaire, G., Harms, F., Idir, M., Huang, L., Levecq, X., Piponnier, M., and Zeitoun, P., "Euv and hard x-ray hartmann wavefront sensing for optical metrology, alignment and phase imaging," *Sensors* 21, 874 (1 2021).
- [19] Goldberg, K. A., Wojdyla, A., Bryant, D., Shi, X., Rebuffi, L., Frith, M., Highland, M., Assoufid, L., Ichii, Y., Inoue, T., and Yamauchi, K., "X-ray wavefront sensor development at the advanced light source," 17, SPIE-Intl Soc Optical Eng (10 2023).
- [20] Gunjala, G., Wojdyla, A., Goldberg, K. A., Qiao, Z., Shi, X., Assoufid, L., and Waller, L., "Data-driven modeling and control of an x-ray bimorph adaptive mirror," *Journal of Synchrotron Radiation* 30, 57–64 (1 2023).
- [21] Rebuffi, L., Shi, X., Qiao, Z., Highland, M. J., Frith, M. G., Wojdyla, A., Goldberg, K. A., and Assoufid, L., "Real-time machine-learning-driven control system of a deformable mirror for achieving aberration-free x-ray wavefronts," Optics Express 31, 21264 (6 2023).

- [22] Xiao, S., Davison, I., and Mertz, J., "Scan multiplier unit for ultrafast laser scanning beyond the inertia limit," Optica 8, 1403 (11 2021).
- [23] Mino, L., Bonino, V., Agostino, A., Prestipino, C., Borfecchia, E., Lamberti, C., Operti, L., Fretto, M., Leo, N. D., and Truccato, M., "Maskless x-ray writing of electrical devices on a superconducting oxide with nanometer resolution and online process monitoring," *Scientific Reports* 7 (12 2017).
- [24] Naulleau, P. P., Goldberg, K. A., Batson, P., Bokor, J., and Denham, P. E., "Fourier-synthesis custom-coherence illuminator for extreme ultraviolet microfield lithography," *Applied Optics* 42, 820–826 (2003).
- [25] Yan, S., Jiang, H., Jiang, Z., Liang, D., Xie, J., Zhu, H., Shu, G., Ben, N., and Li, A., "X-ray speckle reduction using a high-speed piezoelectric deformable mirror system," *High Power Laser Science and Engineering* 13, e22 (1 2025).
- [26] Chen, P., Jung, I. W., Walko, D. A., Li, Z., Gao, Y., Shenoy, G. K., López, D., and Wang, J., "Ultrafast photonic micro-systems to manipulate hard x-rays at 300 picoseconds," *Nature Communications* 10 (12 2019).
- [27] Schmidt, D., Hensel, D., Petev, M. V., Khosla, M., Brede, M., Vadilonga, S., and Gaal, P., "Wavegate: a versatile tool for temporal shaping of synchrotron beams," *Optics Express* **32**, 7473 (2 2024).
- [28] Walker, J., Liu, T., Tendulkar, M., Burrows, D. N., DeRoo, C. T., Allured, R., Hertz, E. N., Cotroneo, V., Reid, P. B., Schwartz, E. D., Jackson, T. N., and Trolier-McKinstry, S., "Design and fabrication of prototype piezoelectric adjustable x-ray mirrors," Optics Express 26, 27757 (10 2018).
- [29] Tendulkar, M. M., Liu, T., Kirchner-Hall, N., Bishop, N. L., Tran, Q., DeRoo, C. T., Cotroneo, V., Kradinov, V., Marquez, V., Reid, P. B., Trolier-McKinstry, S., and Jackson, T. N., "Process development for adjustable x-ray mirrors," in [Optics for EUV, X-Ray, and Gamma-Ray Astronomy X], Pareschi, G., O'Dell, S. L., and Gaskin, J. A., eds., 59, SPIE (8 2021).
- [30] Buffo, K., DeRoo, C., Reid, P., Kradinov, V., Marquez, V., Trolier-McKinstry, S., Bishop, N., Jackson, T. N., Tran, Q., Liang, H., and Tendulkar, M., "Adjustable x-ray optics: thin-film actuator measurement and figure correction performance," *Journal of Astronomical Telescopes, Instruments, and Systems* 10 (8 2024).
- [31] Ronneberger, O., Fischer, P., and Brox, T., "U-net: Convolutional networks for biomedical image segmentation," in [Medical image computing and computer-assisted intervention-MICCAI 2015: 18th international conference, Munich, Germany, October 5-9, 2015, proceedings, part III 18], 234–241, Springer (2015).
- [32] Sherstinsky, A., "Fundamentals of recurrent neural network (rnn) and long short-term memory (lstm) network," *Physica D: Nonlinear Phenomena* **404**, 132306 (2020).
- [33] Gunjala, G., Wojdyla, A., Goldberg, K. A., Qiao, Z., Shi, X., Assoufid, L., and Waller, L., "Data-driven modeling and control of an x-ray bimorph adaptive mirror," *Synchrotron Radiation* **30**(1), 57–64 (2023).
- [34] Bishop, N. L., Kradinov, V., Reid, P. B., Jackson, T. N., DeRoo, C. T., and Trolier-McKinstry, S., "Stress-balancing in piezoelectric adjustable x-ray optics," *Journal of Astronomical Telescopes, Instruments, and Systems* 8(2), 029004 (2022).
- [35] Wang, T., Huang, L., Zhu, Y., Giorgio, S., Boccabella, P., Bouet, N., and Idir, M., "Ion beam figuring system for synchrotron x-ray mirrors achieving sub-0.2-μrad and sub-0.5-nm root mean square," *Nanomanufacturing* and Metrology 6, 20 (12 2023).